Journal of The Electrochemical Society, **149** (4) G286-G296 (2002)
0013-4651/2002/149(4)/G286/11/$7.00 © The Electrochemical Society, Inc.

Enhanced Transport by Acoustic Streaming in Deep Trench-Like Cavities

R. H. Nilson[z] and S. K. Griffiths

Sandia National Laboratories, Livermore, California 94551-0969, USA

High frequency acoustic agitation is known to enhance chemical dissolution rates of patterned photoresists used in semiconductor and LIGA microdevice fabrication. To better understand the physical mechanism of this enhancement, we have developed analytical and numerical models of the acoustically induced steady streaming motion that transports dissolved polymer fragments from the bottom of trench-like features into the developer bath. Analytical solutions describing the time-periodic wave motion are used to evaluate the time-mean Reynolds stresses that drive the steady streaming motion. The resulting steady torroidal flow within the feature is computed by solving the Navier-Stokes equations, including either the acoustic Reynolds stresses or the slip velocity that applies when the acoustic boundary layers are sufficiently thin. The steady velocity field is then used to compute species transport by diffusion and advection. These numerical results are complemented by analytical solutions describing the dependence of enhanced transport on process parameters. The results indicate that acoustic streaming is probably responsible for the observed three to fourfold increase in development rates of LIGA features having widths of a few micrometers or more. To gain the same relative benefit in submicrometer features would, however, require use of frequencies and power levels more than tenfold greater than the conventional levels of 1 MHz and 10 W/cm^2.
 [DOI: 10.1149/1.1459716]

Manuscript received July 1, 2001. Available electronically March 12, 2002.

Fabrication of microelectronic and LIGA microdevices often requires transport of chemical species into or out of liquid-filled microcavities. Two common examples are the chemical development of patterned photoresists to produce recessed features and the filling of such features by electrodeposition. During chemical development, fragments of the resist must be transported from the bottom of narrow features into the development bath. Similarly, filling of a patterned resist by electrodeposition requires transport of metal ions from the electroplating bath into the features. This plating process is commonly used to form microelectronic interconnects having submicrometer linewidths. Although the depths of these features may be several times greater than their widths, they rarely exceed a depth of 1 μm. Over these short length scales, diffusion provides very effective transport of chemical species. Transport rates are, however, smaller by orders of magnitude in the LIGA process used to produce detailed metal parts having depth dimensions of a millimeter or more.

The acronym LIGA is derived from the German words for lithography, electroforming, and molding.[1] In LIGA, a high-energy X-ray source is used to expose a thick photoresist, typically polymethylmethacrylate (PMMA), through a patterned absorber mask. The exposed material is then removed by chemical dissolution in a development bath. This development process yields a nonconducting mold having a conducting substrate beneath deep cavities that are subsequently filled by electrodeposition. The resulting metal parts may be the final product or may be used as injection or embossing molds for mass production.

Development and deposition rates in recessed features depend on both species transport and surface reaction kinetics. Transport is rarely an issue in conventional electroplating on flat surfaces where surface ion concentrations can be maintained by pumping bath fluids or by moving the substrate relative to the bath. However, in plating or development of patterned photoresists, even a very strong external flow is not effective in providing increased transport into recessed features having aspect ratios greater than one or two.[2-4] This is because the convective cell that circulates the fluid in the top of each feature penetrates only about one feature width. Additional counter-rotating convective cells are formed deeper within high aspect ratio features, but the circulation speeds decrease by nearly two orders of magnitude between successive cells.[4] Thus, high aspect ratio features are essentially stagnant over most of their height, while low aspect features are well-stirred throughout. This disparity of transport may lead to faster development or electroplating of wide features relative to narrow ones, causing undercutting adjacent to wider features during development and excessive overplating during deposition.

With increasing feature depth, the path length for diffusion becomes progressively longer, reducing the rate of transport relative to the surface reaction rate. Under these diffusion-limited conditions, very long processing times ranging from many hours to several days are required for development of LIGA features having depths of 1 to 2 mm. Diffusion-limited electrodeposition requires even longer time periods for similar feature sizes, because the maximum available differences in metal ion concentration are three to four orders smaller than the deposit density, whereas these densities are comparable in development.

Acoustic agitation offers a promising means for enhancing transport rates within high aspect ratio features. A number of researchers have demonstrated experimentally that development rates can be increased severalfold by performing the process in acoustic baths like those used for cleaning of semiconductor wafers.[3,5-7] In these previous studies, it is suggested that the collapse of acoustically generated bubbles is responsible for increased development rates. Although the exact mechanism is uncertain, bubble collapse is thought to generate very large local temperatures that increase surface reaction rates.[8] In addition, pressure forces produced by collapsing bubbles may help to dislodge polymer fragments or adsorbed species that are loosely bound to surfaces. However, for the megasonic frequencies used in LIGA, typical acoustic power levels of <100 kW/m^2 (10 W/cm^2) are below the threshold required to produce cavitation.[8,9] Moreover, the fact that LIGA development rates decrease substantially with increasing feature depth even under acoustic agitation strongly suggests that development rates of high-aspect-ratio features are limited by transport within features, not by surface reaction rates. It follows that the principal benefit of acoustic agitation is improved feature-scale transport.

The present paper demonstrates that the observed acoustic enhancement of LIGA development rates can be attributed to acoustic streaming within features. In this mechanism, the steady streaming flow induced by high-frequency agitation circulates most of the fluid within features, substantially increasing species transport. Although the fluid dynamics of acoustic streaming have been studied extensively,[10-12] there have been no previous studies of the induced species transport in cavities and recessed features.

To better understand this process, analytical and numerical methods are used to solve the equations governing flow and species transport within trench-like features. The sound field is described by

[z] E-mail: rhnilso@sandia.gov

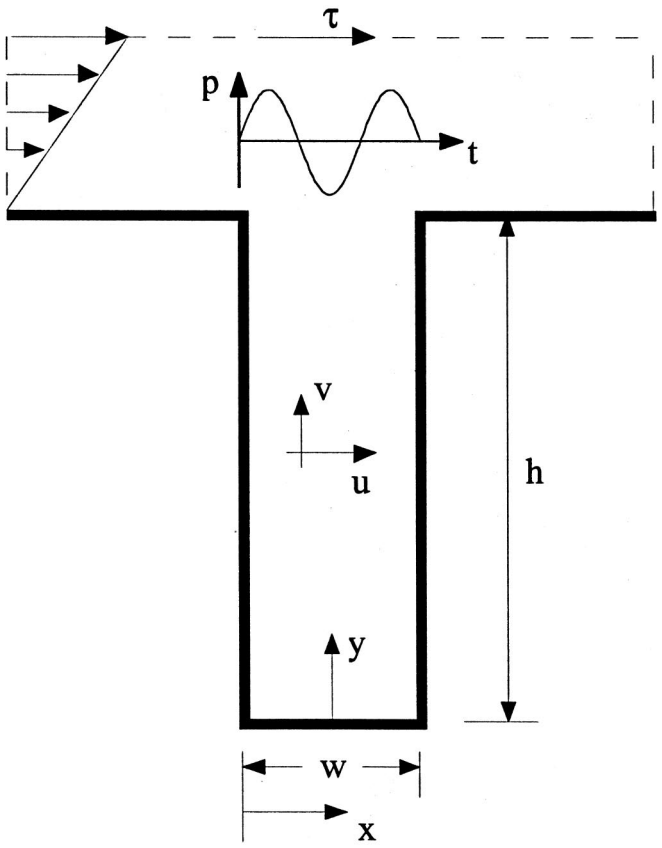

Figure 1. Schematic of a trench-like feature. During development, dissolved polymer fragments are transported from the dissolution front to the feature mouth. In electrodeposition, metal ions are transported from the feature mouth to the feature bottom.

exact solutions derived by Rayleigh[10] and Nyborg.[11] The time-mean Reynolds stresses computed from these harmonic solutions are then used as the driving source terms in a numerical solution of the Navier-Stokes equations. The resulting steady acoustic streaming flow field is finally used to compute the transport of a representative chemical species by diffusion and advection. In addition to these numerical results, we also derive analytical solutions relating transport rates to feature dimensions and processing conditions.

Although acoustic streaming is effective in reducing LIGA development times, model predictions suggest that this mechanism will provide far less benefit to electrodeposition. This is because the diffusivity of metal ions is orders of magnitude greater than that of polymer fragments, reducing the importance of advective transport relative to diffusive transport.

Governing Equations

To model the effects of acoustic agitation in recessed features we consider the simplified geometry of a single trench-like feature as shown in Fig. 1. In the region far above the resist surface, $y \gg h$, the bath is presumed to be well mixed and to have a negligible concentration of dissolved polymer fragments or a uniform concentration of metal ions. Since the frequency, f, and intensity, I, of the sound field are known for commercial acoustic baths, these conditions are used to characterize the pressure variations in the fluid at the feature mouth. For simplicity, the solid feature walls are presumed motionless due to disparity of acoustic impedance or oblique wave incidence. Although the feature height varies during development and deposition, the motion of the feature bottom is sufficiently slow that flow and transport processes may be presumed quasi-steady.

The effects of bath stirring are modeled by prescribing a steady uniform flow from left to right above the resist. This uniform external flow produces a linear gradient of the fluid speed in a boundary layer just above the resist surface. The resulting shear force is transmitted to the fluid at the top of the feature, driving motion within the feature. However, as noted earlier, the effects of this forced convection are negligible when the aspect ratio is large.

The fluid velocity field within the feature is governed by the Navier-Stokes equations. A direct numerical solution of these equations is possible but somewhat impractical because of the large difference in the time scales of acoustic agitation and chemical development. Since the period of a typical 1 MHz acoustic wave is only 1 ms, billions of numerical time steps would be needed to span even a few minutes of development time. To deal with this disparity we utilize a method of successive approximations that has been previously used in solving problems of this general class.[10-12] The pressure, p, density, ρ, and velocity $u = ui + vj$ are each written as an infinite series.

$$p = p_o + p_a + p_s + \ldots \quad \rho = \rho_0 + \rho_a + \rho_s + \ldots$$
$$u = u_a + u_s + \ldots \qquad [1]$$

The ambient values of pressure and density, p_0 and ρ_0, are taken as constant and uniform. The acoustic terms, subscripted a, are assumed to be harmonic functions of time but may vary arbitrarily with position. The steady acoustic streaming terms, subscripted s, are time invariant but are, again, free to vary spatially. These series expansions are substituted into the Navier-Stokes equations and terms of like time dependence are equated to one another. The first-order harmonic terms and their products with p_0 and ρ_0 yield the linearized acoustic equations[10,13]

$$\frac{\partial \rho_a}{\partial t} + \rho_0 \nabla \cdot u_a = 0 \qquad [2]$$

$$\rho_o \frac{\partial u_a}{\partial t} = -\nabla p_a + \mu \nabla^2 u_a + \left(\mu_b + \frac{1}{3}\mu\right)\nabla(\nabla \cdot u_a) \qquad [3]$$

Here, μ and μ_b are the shear and bulk viscosities. The acoustic pressure and density variations are related by the equation of state, $p_a = c^2 \rho_a$, in which c is the speed of sound. As explained later, these equations can be solved by superposing solutions derived by Rayleigh[10] for traveling waves in tubes and channels of infinite length.

The equations governing the acoustic streaming flow are deduced by taking the time average of the series expansion of the Navier-Stokes equations. The averaging process eliminates all of the simple harmonic terms that appeared in the preceding linear acoustic equations but leaves the steady flow quantities, subscripted s below, as well as the time averaged products of harmonic functions that are gathered into F[11]

$$\nabla \cdot u_s = 0 \quad \nabla p_s - \mu \nabla^2 u_s = F \qquad [4]$$

$$F = -\rho_0 \langle (u_a \cdot \nabla) u_a + u_a (\nabla \cdot u_a) \rangle \qquad [5]$$

The steady streaming motion is driven by an apparent body force, F, arising from the Reynolds stresses produced by the harmonic motion. Note that the time averaging brackets, $\langle\ \rangle$, that enclose the Reynolds stresses have been dropped from the time invariant quantities, u_s and p_s, because they are redundant. Although it is essential that compressibility be retained in the acoustic Eq. 2 and 3, the streaming flow may be assumed incompressible. Also, the speed of acoustic streaming is generally so small that the inertia of the streaming motion has been deleted from Eq. 4.

The solution procedure is as follows: solve Eq. 2 and 3 analytically for the harmonic velocity field; evaluate the Reynolds stresses that comprise F; numerically solve Eq. 4 and 5 for the steady

streaming flow. The steady velocity field is then used to numerically solve the conservation equation describing steady diffusive and advective transport of a single species

$$\nabla \cdot (u_s C) = \nabla \cdot (D \nabla C) \quad [6]$$

Here, C is the polymer fragment or metal ion concentration and D is the diffusivity of that species.

Harmonic Velocity Field

High frequency pressure variations at the feature mouth drive the acoustic motion within the feature. Rayleigh[10] derived traveling wave solutions that satisfy the two-dimensional Cartesian form of the acoustic wave equations, Eq. 2 and 3, for a channel bounded by infinite parallel planes, subject to nonslip and impermeable boundary conditions on the bounding walls. These solutions can be applied to the trench-like feature geometry of Fig. 1. The u and v velocity components of the Rayleigh solution are each proportional to the nominal acoustic velocity u_{a0} which is matched to the sound intensity, I, in the bath at the feature mouth. The velocity component along the feature axis is generally orders of magnitude greater than the transverse component. Because of the nonslip condition, thin viscous boundary layers develop interior to the feature along the feature side walls. The viscous boundary layer thickness, δ, is nearly uniform along the feature height. The simple formulas given below can be used to calculate u_{a0}, δ, and the acoustic wave length, λ

$$u_{a0} = \sqrt{\frac{I}{\rho c}} \approx 0.2 \text{ m/s} \quad \delta = \sqrt{\frac{2\mu}{\omega\rho}} \approx 0.6 \ \mu\text{m} \quad [7]$$

$$\lambda = \frac{c}{f} \approx 1.5 \text{ mm} \quad [8]$$

The above numerical estimates are based on a frequency, $f = \omega/2\pi = 1$ MHz, and a sound intensity, $I = 60$ kW/m^2 (6 W/cm^2), typical of commercial wafer cleaning baths, and fluid properties like those of water: $\rho = 1000$ kg/m^3, $c = 1500$ m/s, and $\mu = 10^{-3}$ Pa s. In addition to the scaling constant, u_{a0}, the Rayleigh solution contains three dimensionless parameters, the normalized wave length, λ/w, the aspect ratio, h/w, and normalized thickness of the viscous boundary layers, δ/w. For given choices of these parameters, there are two solutions representing waves traveling in opposite directions along the feature. To obtain the full solution, we must generally superpose the downward traveling wave with its upward traveling reflection off the lower surface.

The reflected wave may strongly influence the velocity field if the feature bottom is highly reflective. This is likely the case in electroplating because the plating surface at the mold bottom has an acoustic impedance much greater than that of the electrolyte. In this instance, the combination of the primary and reflected waves produces a standing wave having increased motion in some locations and reduced motion in others. The corresponding patterns of acoustic streaming are also strongly affected and become cellular in character.[10] In development, however, the polymer surface at the mold bottom has a density and wave speed that typically exceed those of the developer fluid by only about 20% and a factor of two to three, respectively. Under these conditions the impedance mismatch is less severe and the amplitude of the reflected wave is only 20 to 30% as great as that of the incident wave, probably even weaker owing to the partially developed gel layer at the feature bottom. For these reasons and for the sake of simplicity, the reflected wave will not be included in any of the calculations presented here.

Figure 2 shows the computed amplitude of the longitudinal velocity, v_a, along the feature as a function of transverse position for several choices of the normalized boundary layer thickness, δ/w. The solid lines represent the Rayleigh solution explained above

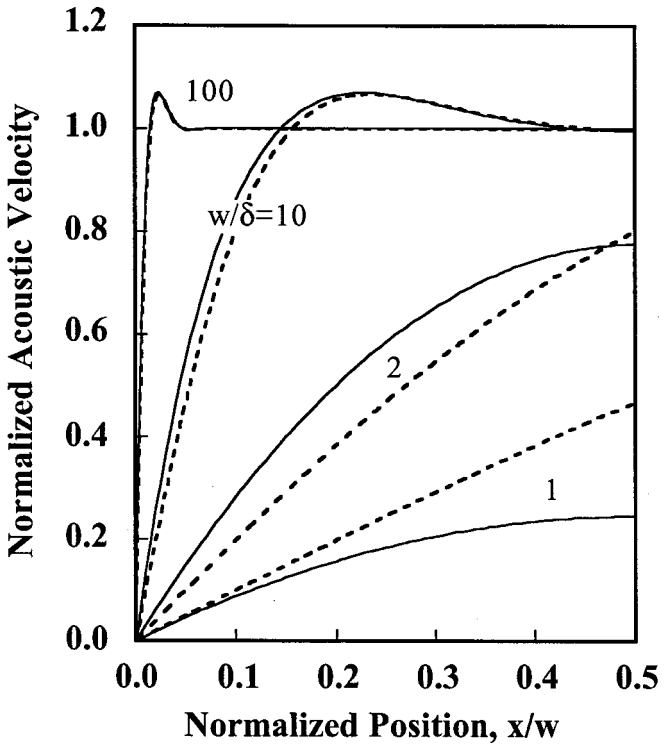

Figure 2. Normalized acoustic velocity, v_a/u_{a0}, at feature top *vs.* normalized transverse position. Feature wall is at left; feature center is at right of plot. Solid lines are exact Rayleigh solution; dotted lines are approximate solution given by Eq. 9 for $\alpha = 0$.

while the dotted lines represent the following approximate solution derived by Nyborg in the limit where the viscous boundary layers are thin compared to the feature width[11]

$$v_a \approx u_{a0}(1 - e^{-(1+j)\,x/\delta}) e^{\pm(\alpha + j\,2\pi/\lambda)y} e^{j\omega t} \quad [9]$$

$$u_a \approx -v_a 2\pi \frac{\delta}{\lambda}\left(\frac{j}{1+j}\right) \quad [10]$$

Here, $j = (-1)^{1/2}$ and the real part of each function is implied. As seen in Fig. 2, the approximate solution provides a very good estimate, provided that $w/\delta > 10$. For agitation at 1 MHz, $\delta \sim 0.6$ μm, so the approximate solution will remain valid and the attenuation moderate for LIGA features having widths of 6 μm or more. A frequency of about 1 GHz will be needed, however, to satisfy the same criteria for semiconductor lines having a width of 0.15 μm. The velocity profiles shown in Fig. 2 are applicable at the mouth of the feature. The attenuation coefficient in Eq. 9, $\alpha = \delta^2(2\pi/\lambda)^3/3$, describes viscous attenuation of a one-dimensional wave in free space and is much weaker than the axial attenuation along a walled feature, as explained below.

In addition to the boundary-layer damping of the motion seen in Fig. 2, there is additional viscous attenuation of the amplitude between the top and bottom of the feature. The two-dimensional Rayleigh[10] solution indicates that for moderate attenuation the pressure and velocity amplitudes decay nearly exponentially such that the ratio of bottom to top amplitudes is $\exp(-\pi h\delta/\lambda w)$. Figure 3 illustrates the attenuation computed from the full solution. It is seen that wave attenuation is insignificant at 1 MHz for millimeter-depth features provided that the feature width is greater than about 10 μm, so this effect is usually negligible in LIGA. Although the attenuation increases at higher frequencies because of reduced wavelength,

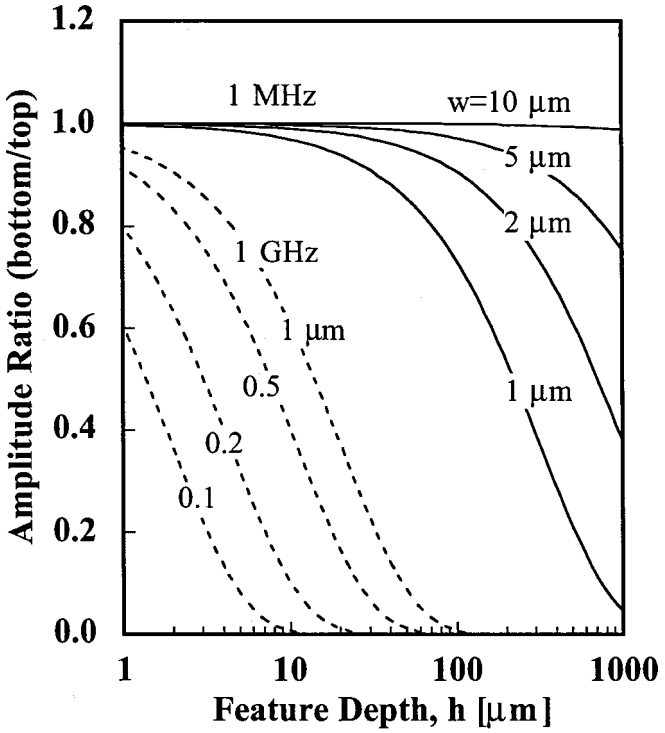

Figure 3. Attenuation of acoustic velocity along feature *vs.* feature depth. At 1 MHz attenuation is unimportant for millimeter-depth features provided that feature width is greater than about 10 μm.

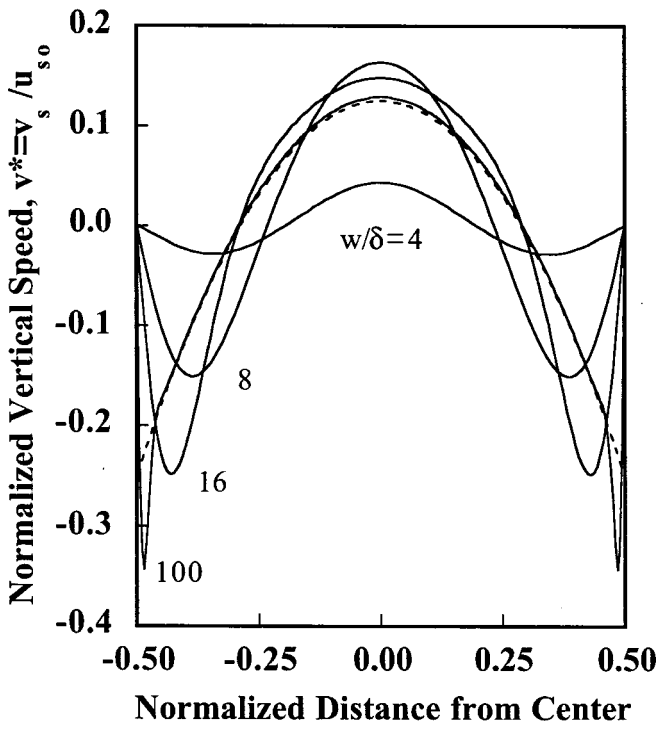

Figure 4. Normalized streaming velocity *vs.* normalized distance from feature center. Dotted line is asymptotic solution for $w/\delta \gg 1$.

acoustic waves with a frequency of 1 GHz are not substantially attenuated in semiconductor lines having widths of 0.25 μm and depths up to 1 μm.

Acoustic Streaming Along Feature

The acoustic streaming motion in deep features having weakly reflective bottoms can be well approximated using an approach suggested by Nyborg.[11] Over most of the height of a slender feature the streaming velocity is nearly vertical, so the transverse velocity component can be neglected to obtain the following simplification of Eq. 4

$$\int_0^w v_s dx = 0 \qquad [11a]$$

and

$$\mu \frac{\partial^2 v_s}{\partial x^2} = \frac{\partial p_s}{\partial y} - F_y \qquad [11b]$$

The driving Reynolds stresses F_y acting in the vertical direction are evaluated by substituting the preceding asymptotic solution of Eq. 9 and 10 into the definition of F in Eq. 5. The velocity profile, $v_s(x)$, is then determined by analytically integrating Eq. 11b across the feature subject to nonslip conditions at the feature walls. In doing this, the vertical pressure gradient is assumed to be constant and is determined by enforcing the above integral constraint, Eq. 11a, that the net vertical flow through any horizontal cross section must be identically zero. These solutions are suggested but are not presented or displayed by Nyborg and so are given below.

Solutions to Eq. 11 may be written in the following form

$$v^* = K_1^* \eta + K_2^* \eta^2 + \frac{1}{4}[1 + 2(S(\eta) - C(\eta)) + e^{-2\eta}] \qquad [12]$$

where

$$v^* = \frac{v}{u_{s0}} = \frac{v c_0}{u_{a0}^2} \quad \eta = \frac{x}{\delta} \quad \hat{\eta} = \frac{w}{2\delta} \qquad [13]$$

$$S(\eta) = e^{-\eta} \sin \eta \quad C(\eta) = e^{-\eta} \cos \eta \qquad [14]$$

$$K_1^* = -2K_2^* \hat{\eta} - C(\hat{\eta}) + \frac{\hat{\eta}}{2} e^{-2\hat{\eta}} \qquad [15]$$

and

$$K_2^* = \frac{3}{4\hat{\eta}^3}\left[\frac{(1 - e^{-2\hat{\eta}})}{4} + \frac{\hat{\eta}}{2} - S(\hat{\eta}) - \hat{\eta}^2\left(C(\hat{\eta}) - \frac{e^{-2\hat{\eta}}}{2}\right)\right] \qquad [16]$$

Here, x may be measured from either wall, with the understanding that the expressions are only valid for $0 < x < w/2$.

The velocity profiles computed from Eq. 12-16 are illustrated in Fig. 4. The downward flow along the feature walls is driven by large Reynolds stress gradients in the acoustic boundary layers adjacent to the walls. The upflow in the center is simply a consequence of continuity. The fluid speeds shown in Fig. 4 are scaled by the nominal acoustic streaming speed

$$u_{s0} \equiv \frac{u_{a0}^2}{c} = \frac{I}{\rho c^2} \approx 27 \ \mu\text{m/s} \qquad [17]$$

The numerical estimate given above corresponds to an acoustic intensity of $I = 60$ kW/m^2 (6 W/cm^2) in a fluid-like water with a density of 1000 kg/m^3, and sound speed, c_o, of 1500 m/s. This steady flow speed is sufficient to traverse a 1 mm feature height in less than 1 min. Note that the nominal streaming speed is independent of viscosity; this is because the driving force F and the resisting shear forces in Eq. 11b are both proportional to the viscosity.

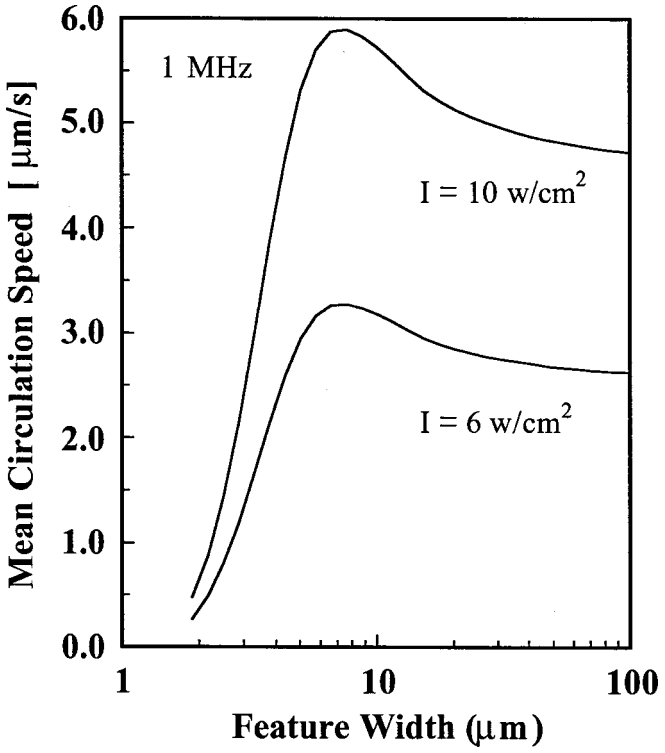

Figure 5. Mean circulation speed *vs.* feature width. Mean speed is computed by averaging vertical velocity profile across downflow region.

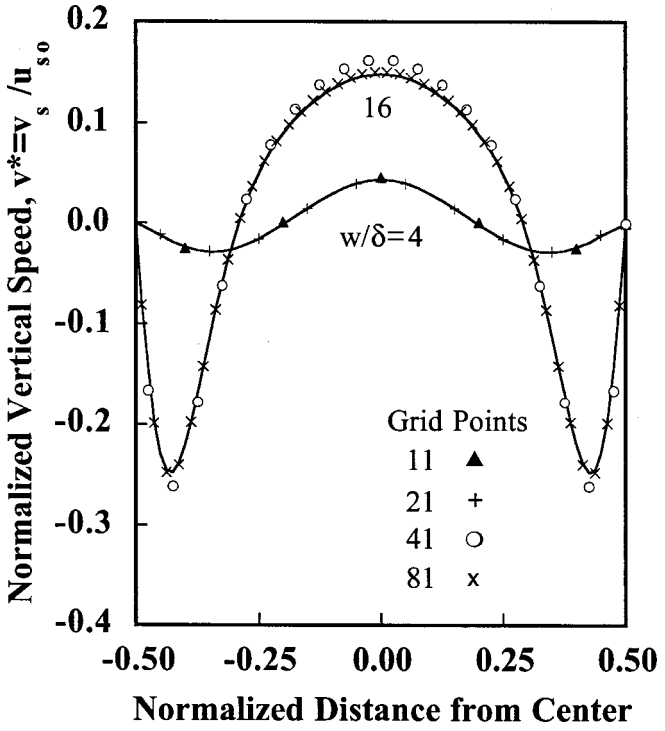

Figure 6. Comparison of numerically calculated velocity profiles (symbols) with analytical solutions of Eq. 12-16 (solid lines). Every other grid point is displayed. Numerical profiles are at midheight. Aspect ratio is four.

The streaming velocity profiles in Fig. 4 are strongly dependent on the parameter, w/δ, representing the ratio of the feature width to the acoustic boundary layer thickness defined in Eq. 7. For ratios less than about four, the motion is severely suppressed by shear stresses that are inversely proportional to the feature width. In the opposing limit of very wide features, $w/\delta \gg 1$, the velocity profile approaches an asymptotic solution having a parabolic shape and a maximum downward speed of $v^* = -0.25$ immediately adjacent to the wall, as indicated by the dotted line in Fig. 4. Since the maximum speed is roughly coincident with the inner edge of the acoustic boundary layer at $x^* \sim \delta/w \ll 1$, the resulting velocity field is equivalent to that driven by a slip velocity of magnitude $v^* = -0.25$ applied on the vertical walls. This limiting solution often provides a good approximation in practical applications like the LIGA examples presented here.

In narrow features, viscous forces may strongly reduce acoustic streaming speeds, as illustrated in Fig. 5. Here, the vertical axis displays the average fluid speed in the downflow region of the feature for a fixed agitation frequency of 1 MHz and for two acoustic intensities. The streaming motion becomes very weak for a feature width of 2 μm or less; beyond this point the micrometer-scale acoustic boundary layers overlap one another. The final approach to a zero mean speed is not shown in Fig. 5 because it cannot be accurately constructed using Reynolds stresses derived from the approximate acoustic velocity profiles given by Eq. 9 and 10. As seen by comparing solid and dotted lines in Fig. 2, this approximation is inaccurate for w/δ of less than about five. For smaller w, it is necessary to utilize the full Rayleigh solution in computing the Reynolds stresses and streaming speed. Although this can still be done analytically, a more general numerical approach is generally needed to deal with corner regions and species transport. For these reasons we turn now to numerical analysis.

Species Transport: Numerical Model

Numerical methods are used to investigate the transport of polymer fragments or metal ions induced by acoustic streaming in trench-like features. The Navier-Stokes Eq. 4 and 5 governing the streaming motion are rewritten in terms of the stream function and vorticity, as appropriate for steady incompressible flows.[4,14] These equations and the species transport equation, Eq. 6, are discretized using second-order finite differences to obtain a system of algebraic equations for nodal point values of the stream function, vorticity, velocity components, and species concentration.[4,14] These equations are solved iteratively on a rectangular mesh covering the T-shaped domain shown in Fig. 1. In each solution, iterations were continued until the solution was converged on successively finer meshes containing 21, 41, 81, and, if needed, up to 321 grid points across the feature width. Since viscous and concentration boundary layers are present in a number of locations, the rectangular grid was equally spaced in both directions and in all locations.

Although the numerical model had been previously tested for a variety of flow conditions, additional tests were performed to verify that acoustic streaming was correctly computed. As seen in Fig. 6, streaming velocities computed numerically are in good agreement with the analytical solutions shown previously in Fig. 4, provided that the acoustic boundary layers are resolved by several grid points. Although this is easily done for cases with $w/\delta <$ 10-20, it becomes very wasteful for larger values of w/δ. For $w/\delta \gg 1$ the transport can, however, be accurately and efficiently calculated by applying a slip velocity of $u_{so}/4$ on the vertical walls rather than explicitly including the Reynolds stresses comprising F in Eq. 5.

To reduce the number of solution parameters, the position coordinates were scaled by the feature width, w, the velocity components by D/w, and the stream function and vorticity by D and D/w^2, where D is diffusivity of the transported species. The species concentration is scaled by its overall variation, such that the normalized concentrations in the bath and feature bottom are simply zero and unity. The resulting equations contain three dimensionless parameters, the Peclet number, aspect ratio, and normalized thickness of the acoustic boundary layer

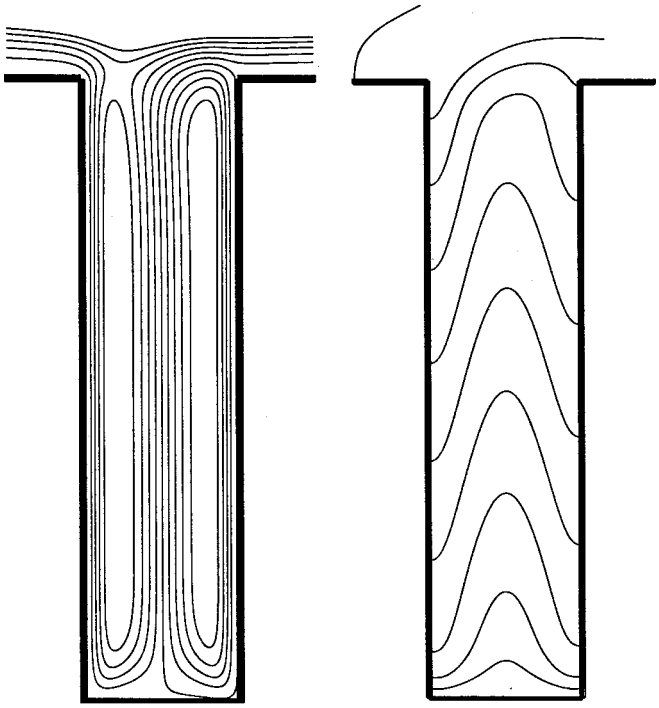

Figure 7. Computed streamlines (left) and isopleths (right) for a Peclet number of $Pe_w = 125$, an aspect ratio of $A = h/w = 4$, and boundary layer thickness of $\delta/w = 1/16$.

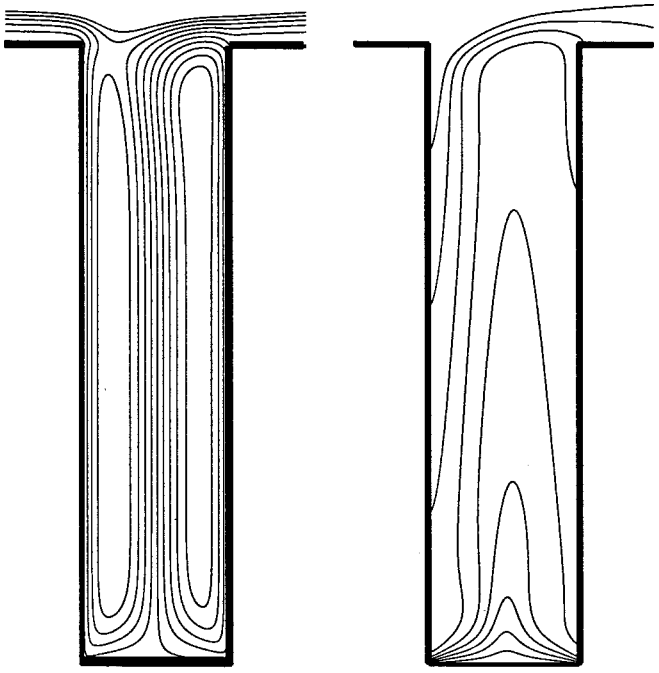

Figure 8. Computed streamlines (left) and isopleths (right) for Peclet number of 500 and aspect ratio of $A = h/w = 4$. Flow is driven by slip velocity on walls.

$$Pe_w = \frac{u_{s0}w}{D} \quad A = \frac{h}{w} \quad \delta^* = \frac{\delta}{w} \qquad [18]$$

The Peclet number, Pe_w, indicates the relative strength of convective transport by acoustic streaming compared to transport by diffusion; it is proportional to the nominal streaming speed, u_{s0}, explained previously. When slip velocities are applied to the feature walls the normalized slip speed is simply $Pe_w/4$. When Reynolds stress are used to drive the motion, solutions also depend on δ/w. In either case, the normalized flow speed across the top of the T-shaped domain of Fig. 1 is taken as equal to the nominal streaming speed within the feature, a very slow speed relative to the bath scale. In the absence of additional stirring, an acoustic streaming motion of roughly this magnitude would occur along the resist face and, as noted earlier, is of little importance for features having aspect ratios greater than two or three.

The most important result of the numerical calculations is the Sherwood number, Sh, representing the ratio of the computed vertical species transport to that which would have occurred by diffusion alone. Under quasi-steady conditions, Sh is the same at all elevations within the feature. It is most conveniently calculated at the feature bottom where the vertical velocity is zero and the transport occurs locally by diffusion alone

$$Sh = \left(\frac{h}{D\Delta C}\right)\frac{1}{w}\int_0^w D\frac{\partial C}{\partial y}dx = A\int_0^1 \frac{\partial C^*}{\partial y^*}dx^* \qquad [19]$$

The value of ΔC used in this formula is the difference between the horizontal mean concentrations at the feature top and bottom. In the absence of fluid motion, the normalized gradient at the bottom is $1/A$ and Sh is unity. In the presence of acoustic streaming, advective transport sweeps fresh developer across the feature bottom, producing a steeper boundary-layer gradient.

Figures 7 and 8 illustrate the computed flow and transport within features having an aspect ratio of four for two different choices of the Peclet number. These two choices correspond to development of LIGA features having widths of 30 and 120 μm at an acoustic power level of $I = 100$ kW/m^2 (10 W/cm^2), assuming a polymer fragment diffusivity of $D = 10^{-11}$ m^2/s. Streamlines are shown on the left side of each figure. Isopleths, lines of constant species concentration, are shown on the right side. The flow within the feature is torroidal with downflow along the walls and upflow in the center. The flow turns at the feature top and bottom over regions having a vertical extent of about one-half feature width. Some of the flow coming in from the left along the resist surface descends into the feature, returns up the center, and rejoins the external flow. As noted previously, the overall transport is not strongly influenced by the flow over the feature top.

The flow along the midsection of the feature does not vary with elevation and is nearly identical to the analytical solutions shown earlier in Fig. 4. With increasing aspect ratio, the flow along the midsection remains the same but extends over a larger fraction of the feature. The turning regions at the ends are not, however, affected by changes in the aspect ratio for aspect ratios greater than two or three.

The streamlines of Fig. 7 and 8 are nearly identical even though the calculation of Fig. 7 was driven by Reynolds stresses in the boundary layers, whereas the flow in Fig. 8 is driven by a slip velocity at the wall. Because of this difference, the streamlines of Fig. 8 are more closely spaced near the walls, indicating slightly higher speeds adjacent to the walls. The relative thickness of the acoustic boundary layer in Fig. 7 is taken as $\delta/w = 1/16$, somewhat thicker than typical of LIGA. A smaller choice of δ/w and identical Peclet numbers would have provided even closer agreement between the streamline patterns in Fig. 7 and 8.

The isopleths on the right of Fig. 7 and 8 are swept downward by descending flow adjacent to the feature walls. Upward flow in the center is also apparent. The close spacing of the isopleths near the feature bottom is indicative of the large diffusion flux at the lower surface. The Sherwood number for the conditions of Fig. 7 is about 3.5, indicating a three- to fourfold enhancement of species transport relative to diffusion.

The fourfold increase in Peclet number between Fig. 7 and 8

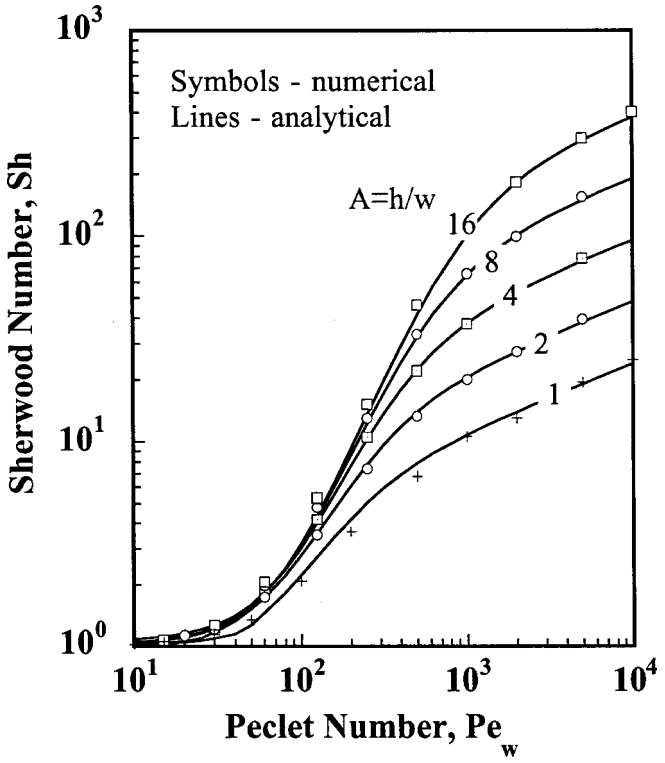

Figure 9. Variation of Sherwood number with Peclet number for several aspect ratios. Symbols are numerical results; solid lines are based on analytical transport model.

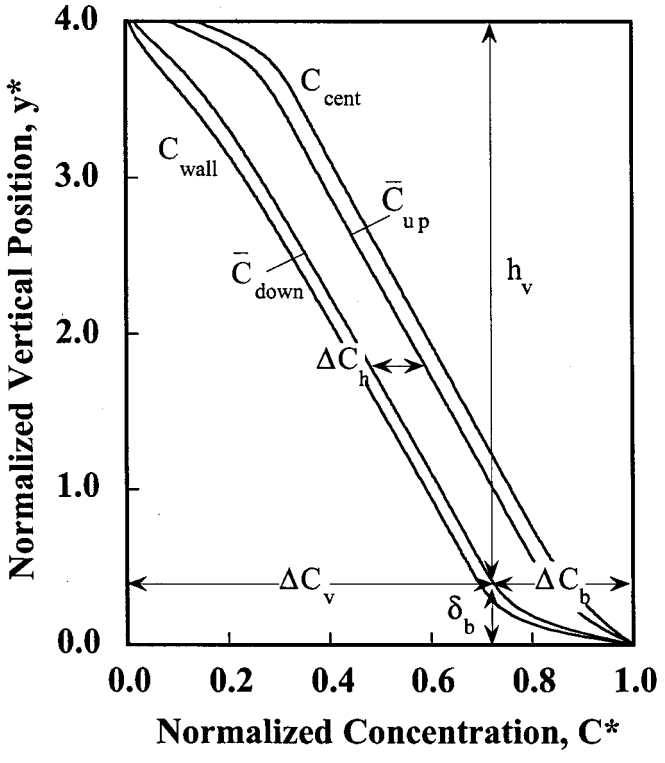

Figure 10. Vertical concentration profiles are nearly linear over the central portion of feature. The difference in concentration between streams is nearly uniform over the central section.

strongly effects the species concentration field. The stronger downflow sweeps the isopleths more steeply downward. Very large concentration gradients at the feature bottom indicate large species fluxes. The fourfold increase in Peclet number between Fig. 7 and 8 results in nearly a sixfold increase in Sherwood number from 3.5 to about 22.

Figure 9 shows the computed variation of the Sherwood number with the Peclet number for several values of the aspect ratio. In all cases the acoustic boundary layer is assumed thin compared to the feature width, permitting the application of the slip boundary condition, $v^* = Pe_w/4$ along the vertical feature walls. For Peclet numbers less than about 10, the Sherwood number is essentially unity, indicating negligible enhancement of transport over diffusion. The deviation of the Sherwood number from unity increases with the square of the Peclet number up to a Peclet number of about 200 to 400. In this regime there is little dependence on the aspect ratio, particularly for aspect ratios of two or more. At higher Peclet numbers, however, *Sh* increases with the third root of Pe_w and is linearly dependent on the aspect ratio. Analytical expressions for these asymptotic regimes and for the smooth curves shown in Fig. 9 are derived in the next section.

Another conclusion drawn from Fig. 9 is that acoustic agitation will not provide significant benefits in electrodeposition. This is because Peclet numbers based on typical metal ion diffusivities of 10^{-9} m^2/s will be no greater than 10 for typical acoustic streaming speeds [$u_{s0} < 40$ μm/s for $I < 100$ kW/m^2 (10 W/cm^2)] and feature widths of 100 μm or less. As seen in Fig. 9, the corresponding Sherwood number is not much greater than unity. In development, however, polymer fragment diffusivities are orders of magnitude smaller, thereby increasing the relative importance of acoustic agitation.

Analytical Transport Model

The preceding numerical solutions are now used to guide the development of analytical solutions relating the Sherwood number to the Peclet number, aspect ratio, and acoustic boundary layer thickness. To this end, we observe that the acoustic streaming flow in a trench-like feature typically produces a vertical concentration profile like that shown in Fig. 10. At the feature bottom there is a boundary layer of thickness, δ_b, over which the concentration varies by an amount ΔC_b. With increasing Peclet number this diffusion layer becomes thinner while the concentration difference across it, ΔC_b, grows larger. Over the remaining height of the feature, denoted h_v, the concentration profiles in the upflow and downflow streams vary almost linearly with height, each having a slope $\Delta C_v/h_v$. Thus, as seen in Fig. 10, the horizontal concentration difference between streams, ΔC_h, is nearly the same at every height.

The relationship between the vertical and horizontal concentration differences can be deduced by averaging the species transport equation, Eq. 6, horizontally across one of the downflow streams to obtain

$$\frac{w}{2}\rho\alpha\left(\overline{V}\frac{d\overline{C}_d}{dy} + D\frac{d^2\overline{C}_d}{dy^2}\right) = \rho D\frac{(\overline{C}_d - \overline{C}_u)}{(w/4)} \qquad [20]$$

Here, α is the fraction of the half-width, $w/2$, occupied by the downflow stream, $\overline{V}$ is the absolute value of the mean downflow speed, and $\overline{C}_d$ and $\overline{C}_u$ are the mean concentrations in the downflow and upflow streams at any elevation. The right side of Eq. 20 accounts for the horizontal diffusion between the adjacent counterflowing streams separated by a mean distance $w/4$. A similar equation can be written for the upflow stream. Both are satisfied by linear solutions having vertical slopes proportional to the horizontal concentration difference between the two streams, $\Delta C_h = \overline{C}_d - \overline{C}_u$

$$\frac{d\overline{C}_d}{dy} = \frac{d\overline{C}_u}{dy} = \frac{\Delta C_v}{h_v} = \frac{8D}{\alpha\overline{V}w^2}\Delta C_h \qquad [21]$$

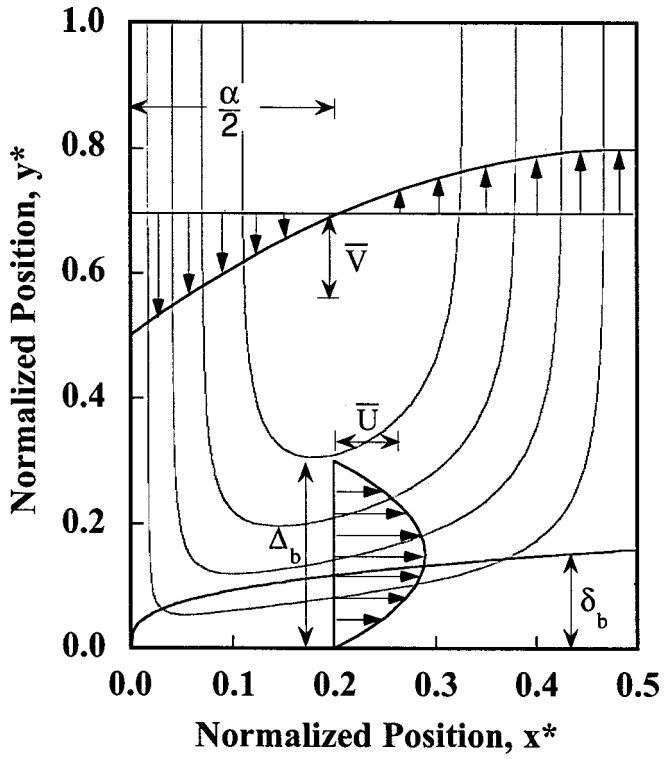

Figure 11. Schematic of turning flow near feature bottom superposed on computed streamlines. Only left half of feature bottom is shown. Flow field is nearly independent of Peclet number and aspect ratio for $A > 1$.

When the acoustic boundary layers are sufficiently thin, as assumed in our example calculations, the vertical velocity profile is parabolic in form with a maximum downflow speed of $V_{max} = u_{so}/4$ adjacent to the walls, as explained earlier. Integration of this profile yields a mean downflow speed of $\overline{V} \sim 0.4\ V_{max}$ over a downflow region spanning a fraction, $\alpha = 1 - 1/\sqrt{3} \sim 0.42$, of the feature half-width, as indicated schematically in Fig. 11. However, the transport analysis is not limited to these asymptotic relations, as Eq. 12-16 can be used to deduce the corresponding values of α and $\overline{V}$ for any choice of δ/w.

The vertical diffusion flux through the boundary layer at the feature bottom must be in balance with the combined diffusive and advective fluxes through the midsection, leading to the relationship

$$mD\frac{\Delta C_b}{\delta_b} = D\frac{\Delta C_v}{h_v} + \alpha\overline{V}\Delta C_h \qquad [22]$$

in which the last term is based on the observation that the upward and downward streams have identical volume flows, both equal to $\alpha\overline{V}$, but have species concentrations differing by ΔC_h. The parameter m appearing just above is unity when the fluid motion is insignificant and, hence, the vertical concentration profile is everywhere linear. At high Peclet numbers, however, the concentration profile near the bottom becomes more nearly quadratic with a slope at the surface about twofold greater ($m = 2$) than the mean slope. Combining the preceding Eq. 21 and 22 and noting that $\Delta C_b = \Delta C - \Delta C_v$, yields

$$\frac{\Delta C_v}{\Delta C} = m\frac{h_v}{\delta_b}\left(\frac{\alpha^2}{8}\overline{Pe}^2 + 1 + m\frac{h_v}{\delta_b}\right)^{-1} \qquad [23]$$

where $\overline{Pe}$ is a Peclet number based on the mean vertical speed

$$\overline{Pe} = \frac{\overline{V}w}{D} = Pe_w\frac{\overline{V}}{u_{s0}} \sim Pe_w\frac{0.4}{4} \qquad [24]$$

At high Peclet numbers, the thickness, δ_b, of the diffusion layer at the feature bottom is controlled by the horizontal flow across the bottom surface, as shown schematically in Fig. 11. The boundary layer growth in crossing the feature half width is estimated by substituting a parabolic concentration profile into the following integral form of the transport equation applicable to a thin concentration boundary layer

$$\frac{d}{dx}\int_0^{\delta_b} u\Delta C_b\left(1 - \frac{y}{\delta_b}\right)^2 dy = D\left.\frac{\partial C}{\partial y}\right|_{y=0} = 2D\frac{\Delta C_b}{\delta_b} \qquad [25]$$

Again, for high Peclet numbers, the concentration boundary layer lies well within the bottom shear layer. Under these conditions the velocity profile is essentially linear over the integration range of Eq. 25 and may be written as $u = (\tau/\mu)y$. The shear stress τ is estimated by assuming that the flow across the bottom is parabolic in form with a mean speed $\overline{U}$ and a maximum of $3\overline{U}/2$ at a distance $\Delta_b/2$ above the floor. Further, since the vertical down flow must be in balance with the horizontal flow across the bottom, it follows that $\overline{U}\,\Delta_b = \overline{V}\alpha w/2$. Finally, the horizontal mean of the boundary layer thickness, δ_b, is determined by performing the above integration in y, solving the resulting differential equation for $\delta_b(x)$, averaging across the bottom and making a few algebraic substitutions

$$\frac{\delta_b}{w} = \frac{3}{4}\left[\frac{6}{\alpha}\left(\frac{\Delta_b}{w}\right)^2\frac{1}{\overline{Pe}}\right]^{1/3} \approx 0.83\overline{Pe}^{-1/3} \qquad [26]$$

The above numerical value of 0.83 is based on the observation that $\Delta_b/w \sim 0.3$, as apparent in Fig. 11. Note that this ratio depends mainly on the Reynolds number, $Re = u_{s0}w/\nu$, which is asymptotically small for the acoustic streaming flows of interest here. So Eq. 26 should provide a good approximation provided that the Peclet number is large and that $h \gg \Delta_b$, or equivalently $A = h/w \gg 1/3$.

At small values of the Peclet number, the thickness of the diffusion boundary layer is of little importance because the transport along the full feature height, including the boundary layer, is by diffusion alone. In this limit we arbitrarily take the boundary layer thickness, δ_b, as $h/2$. Further, since the high-Peclet estimate of Eq. 26 may yield unphysical values of δ_b greater than $h/2$ for small Pe, it is convenient to simply define δ_b as the lesser of the high and low Pe estimates, as explained further below. A smoother transition between the limits provides only minor benefit at the cost of greater complexity.

The Sherwood number is computed for any specific case by performing the following sequence of calculations. The nominal streaming speed, u_{s0}, is computed from the acoustic intensity using Eq. 7. The mean vertical speed and fractional downflow area are determined from Eq. 12-16 or, for thin acoustic boundary layers, simply taken as $\overline{V} = 0.4u_{a0}/4$ and $\alpha = 0.4$. The Peclet number based on this mean speed, $\overline{Pe}$ from Eq. 24, is then inserted into Eq. 26 to obtain the concentration boundary layer thickness which applies at large Pe. Since this thickness exceeds the trench height for small enough Pe, we require that δ_b be less than $h/2$. This limiter is only active under diffusion-dominated conditions where the analytical model reduces to series diffusion through boundary and central layers having identical diffusivity. The parameter m, describing the transition from linear to quadratic boundary layer profiles, is computed using the formula

$$m = 2 - \exp\left[1 - \left(\frac{h}{2\delta_b}\right)^2\right] \qquad [27]$$

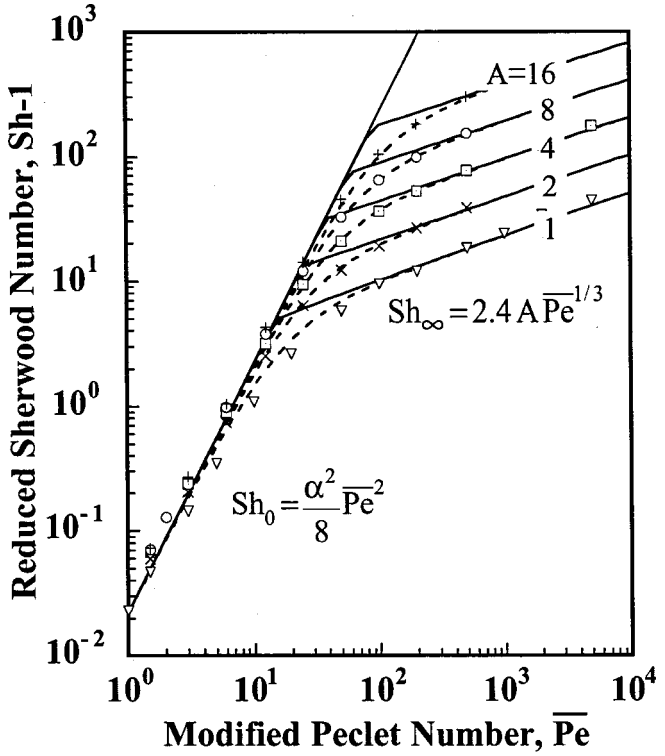

Figure 12. Comparison of asymptotic solutions (solid lines) with numerical calculations (symbols). Dotted line indicates composite formula of Eq. 31.

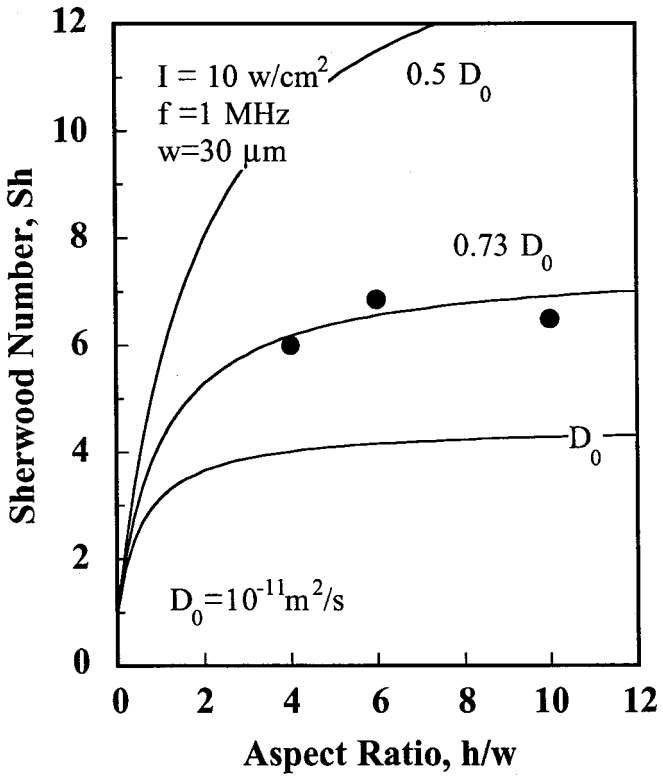

Figure 13. Comparison of analytical model (solid lines) with enhancement of development rates (symbols) observed by Zanghellini *et al.*[3] The Peclet number corresponding to the experimental conditions is 125 for a polymer fragment diffusivity of 10^{-11} cm^2/s.

such that m rapidly changes from 1 to 2 as the boundary layer thickness decreases below the maximum permissible value of $h/2$. The details of these limiting and transitional formulas are not critical to the outcome. The computed values of $\overline{Pe}$, δ_b, m, and $h_v = h - \delta_b$ are finally inserted into Eq. 23 to obtain ΔC_v and these results are used to compute the Sherwood number

$$Sh = \frac{h}{\Delta C}\left.\frac{\partial C}{\partial y}\right|_{y=0} = m\frac{h}{\delta_b}\frac{\Delta C_b}{\Delta C} = m\frac{h}{\delta_b}\left(1 - \frac{\Delta C_v}{\Delta C}\right) \quad [28]$$

The previously discussed Fig. 9 illustrates the excellent agreement between the analytical model of this section and the numerical results of the preceding section.

The asymptotic behavior of the Sherwood number is quite simple in the limits of both small and large Peclet number. It is seen in Fig. 12 that results for all values of the aspect ratio follow nearly the same line for small to moderate values of the Peclet number

$$Sh_0 = \lim_{Pe\to 0}(Sh - 1) = \frac{\alpha^2}{8}\overline{Pe}^2 \quad [29]$$

This relationship can be derived by taking the ratio of the convective and diffusive terms on the right side of Eq. 22, thereafter using Eq. 21 to eliminate $\Delta C_v/\Delta C_h$. Similarly, the large Pe asymptotes are readily deduced from Eq. 23 by taking $\Delta C_b \sim \Delta C$ and using Eq. 26 to define δ_b

$$Sh_\infty = \lim_{Pe\to\infty}(Sh - 1) = m\frac{h}{\delta_b}\frac{\Delta C_b}{\Delta C} \approx 2.4\,A\,\overline{Pe}^{1/3} \quad [30]$$

Based on these asymptotic formulas one can also construct a simple but accurate composite approximation of the form

$$Sh = 1 + \frac{Sh_0 Sh_\infty}{Sh_0 + Sh_\infty} \quad [31]$$

in which the subscripts refer to the above limiting forms. The accuracy of this composite expression is indicated by the dotted lines shown in Fig. 12.

Application to LIGA Development

To our knowledge, the data most relevant to the present study is that of Zanghellini *et al.*[3] In Fig. 3 of that paper the authors present measured LIGA development rates for 30 μm features developed with and without acoustic agitation. By taking the ratio of these two measured rates we obtain a relatively direct estimate of the Sherwood number representing the ratio of transport rates with and without agitation. In doing this we use as our divisor the measured development rates they characterize as dip developed with no bath stirring. These conditions should approximate diffusion-limited development.

It is important to note that our present use of Zanghellini's data presumes that the measured development rates are limited mainly by transport, not by surface dissolution kinetics. This assumption is supported by the fact that observed developments rates are strongly influenced by stirring and agitation. However, to better address this issue, work is in progress to combine the present transport model with a surface kinetics model.

The three data points shown in Fig. 13, for aspect ratios from four to ten, cover the full range for which the authors reported data for both dip and agitation experiments. It is seen that the data (symbols) and calculations (lines) for the two larger values of the diffusivity suggest that the Sherwood number is relatively insensitive to the aspect ratio, consistent with the low Peclet number results shown earlier in Fig. 9 and 12. The variation in the comparative experimental data could easily result from inaccuracy in our reading of the plotted experimental data.

The measurements shown by symbols in Fig. 13 are compared with theoretical calculations for three different choices of the un-

known polymer fragment diffusivity. The other parameters used in the calculations are the experimental intensity and frequency of agitation of 100 kW/m^2 (10 W/cm^2) and 1 MHz. These are the only important parameters, since the acoustic boundary layers are thin compared to the feature width, even for development fluids tenfold more viscous than water. The computed curves are labeled with values of the polymer fragment diffusivity around 10^{-11} m^2/s that bring the calculations into agreement with the measured data. These diffusivities are about 100-fold smaller than those of metal ion species in plating baths. Although we do not have accurate estimates of polymer fragment diffusivities, the order of 10^{-11} m^2/s is quite reasonable for polymer fragments with molecular weights in the thousands,[15] as expected in LIGA. The data presented by Zanghellini *et al.*[3] for dip development rates can be used to estimate the product of the diffusivity and the polymer fragment concentration at the development surface. Based on this product and a diffusivity of 10^{-11} m^2/s, the polymer fragments comprise about 30% of the bulk fluid density at the feature bottom, a reasonable outcome.

Zanghellini *et al.*[3] also report development rates for features ranging from 30-300 μm in a bath having an acoustic intensity of 20 kW/m^2 (2 W/cm^2), five times less than that used in the experiments shown in Fig. 13. Since the Peclet number would then be five times smaller than before, Fig. 9 suggests that there would be relatively little acoustic enhancement in the 30 μm features, but that wider features may still be enhanced. The data appear to show this trend for smaller feature depths, though the variation diminishes as depths grow larger. Similar data is reported by El-Kholi *et al.*[5] We are currently undertaking further analysis of these data sets.

Application to Submicrometer Features

A number of experimental studies have explored acoustic enhancement of photoresist development in features having widths of 10-50 nm (0.01-0.05 μm) using agitation frequencies ranging from 25 to 400 kHz.[6,7] At these low frequencies, the acoustic boundary layer thicknesses computed from Eq. 7 are considerably greater than the feature widths. Under these conditions with $w/\delta < 1$, it is seen in Fig. 4 that the streaming motion within features is very weak. Thus, it is likely that the observed enhancement of development rates in these submicrometer features resulted from bubble collapse rather than acoustic streaming.

The intensity of bubble collapse is enhanced at low frequencies because the longer period of the acoustic cycle permits greater growth and hence stronger collapse during each cycle.[8,9] Shallow feature depths also increase the importance of bubble collapse occurring at the wafer face because there is less attenuation of the induced pressure waves along the feature. For these reasons, it is likely that the low-frequency enhancement of development observed in narrow features is driven by bubble collapse. However, it is also well known that bubble collapse can easily damage fragile parts, and it appears that the associated increases in development rates by this mechanism are not as great as those attainable in LIGA by acoustic streaming.

The submicrometer features typical of semiconductor applications can, according to our analysis, be effectively penetrated by acoustic streaming if the frequency of agitation is raised to about 1 GHz. At this frequency the acoustic boundary layer thickness is of the order 0.02 μm, much smaller than the width of present generation 0.15 μm features. For this boundary layer thickness and the corresponding wave length of 1 μm, the relative wave amplitude at the feature bottom is estimated as $\exp(-\pi h\delta/\lambda w) \sim 0.8$ for an aspect ratio of $h/w = 4$. Thus, at 1 GHz, the fluid streaming speed at the bottom of a submicrometer feature may still be on the order of 30 μm/s for an acoustic intensity of 60 kW/m^2 (6 W/cm^2), just as in the much wider features typical of LIGA. Although the attenuation over the micrometer-scale feature depth may be small, even at gigahertz frequencies, there may be significant attenuation in the region between the driving transducer and the wafer face.

Furthermore, even though the streaming motion in submicrometer features may be strong, the associated advective transport may still be small compared to diffusion. This is not because advection is weak, but rather that the diffusion flux is so large in small features. For example, at a nominal acoustic intensity of 100 kW/m^2 (10 W/cm^2), the Peclet number, $Pe_w = u_{s0}w/D$, is only about 0.5 for a feature width of $w = 0.15$ μm and a fragment diffusivity of 10^{-11} m^2/s. Thus, a 100-fold increase in acoustic intensity to 10^4 kW/m^2 (1 kW/cm^2) would be needed to raise the Peclet number to 50, as required to achieve advective transport twofold greater than diffusion. Larger diffusivities would require even larger power levels. Even if such power levels could be achieved, the associated heating and pressure forces would probably be excessive. Fortunately, the need for acoustic enhancement is greatly reduced for micrometer-depth semiconductor features, since diffusion rates are inversely proportional to the feature depth and diffusion-limited processing times are inversely proportional to the square of the depth. Thus, the need for enhancement is much less than in millimeter-depth LIGA features.

Conclusions

Although acoustic agitation is known to increase photoresist development rates in LIGA and microelectronics applications, the physical mechanism of this enhancement is not well understood. At frequencies less than 100 kHz and at submicrometer feature scales, the collapse of acoustic bubbles may play a role in removing and transporting polymer fragments from the developing surface. However, the megasonic frequencies used in LIGA development are too high to permit cavitation at conventional power levels. Moreover, even if the high-frequency motion does promote surface dissolution, this increase in surface kinetics cannot explain the observed enhancement of development in deep, high-aspect-ratio features. Here, developments rates are limited by fragment transport along the feature rather than surface dissolution kinetics.

The thesis of the present paper is that the observed enhancement of LIGA development rates results from the acoustic streaming process that circulates most of the fluid within high-aspect-ratio features, substantially increasing polymer fragment transport. In support of this hypothesis, analytical and numerical methods have been used to solve the equations governing flow and transport induced by acoustic agitation within trench-like LIGA features. Exact solutions derived by Rayleigh[10] and Nyborg[11] were used to represent the acoustic wave fields within features, including the viscous boundary layers adjacent to feature walls.

Reynolds stresses produced by the high frequency motion induce a steady streaming motion downward along the feature walls at speeds on the order of 30 μm/s. This downward flow is balanced by an upward flow of comparable speed along the feature center. The resulting bidirectional flow along the midsection of high-aspect-ratio features was described using analytical solutions of the one-dimensional Stokes flow equations.

Polymer fragment transport along typical LIGA features was computed by numerically solving the Navier-Stokes equations together with a species transport equation accounting for fragment diffusion and advection. These numerical results were used to guide the development of a physically based analytical model that yields transport rates in terms of Peclet number, feature aspect ratio, and acoustic boundary layer thickness. The limiting forms of the analytical model for low and high Peclet numbers were derived and combined to construct a simple but accurate composite formula describing the Sherwood number for all Peclet numbers.

It was found that the two- to fourfold enhancement in LIGA development rates observed by Zanghellini *et al.*[3] is consistent with model calculations based on a diffusivity of about 10^{-11} m^2/s, a reasonable value for the large polymer fragments produced by PMMA dissolution.[15] The acoustic streaming model further suggests a relatively weak variation of development rate with aspect ratio, in agreement with the Zanghellini data. For the experimental range of Peclet numbers, diffusion-limited development rates increase with

the acoustic intensity and with feature size, again consistent with Zanghellini's data.

It is concluded that acoustic streaming is probably the operative mechanism of acoustic enhancement in development of high-aspect-ratio LIGA features having widths greater than about 1 μm. However, acoustic streaming should not provide much benefit to LIGA electroplating because the metal ions transported into the feature during electroplating are much smaller and more mobile than the polymer fragments transported out of the feature during development. Thus, transport by acoustic streaming is large compared to polymer fragment diffusion but small compared to metal ion diffusion. Similarly, acoustic streaming offers little benefit at the submicrometer scale of microelectronic features because diffusive transport grows stronger with decreasing length scales. Thus, at submicrometer length scales, diffusion alone is sufficient to provide strong transport and moderate processing times.

The results reported here are based on a fundamental, though idealized, model of transport by acoustic streaming. Further work is required to explore acoustic coupling of the bath to the feature and the role of wave reflections from the feature bottom. Additional data is also needed to support model validation. The ultimate goal of this work is the use of physically based models to improve process uniformity, reduce processing times, and extend the range of LIGA fabrication to smaller feature sizes and higher aspect ratios

Acknowledgments

This work was supported in part by the Sandia Materials Science Research Foundation and by the Sandia Accelerated Strategic Computing Initiative. Sandia is a multiprogram laboratory operated by Sandia Corporation, a Lockheed Martin Company, for the United States Department of Energy under contract DE-AC04-94AL85000.

Sandia National Laboratory assisted in meeting the publication costs of this article.

References

1. E. W. Becker, W. Ehrfeld, P. Hagmann, A. Maner, and D. Munchmeyer, *Microelectron. Eng.*, **4**, 35 (1986).
2. K. M. Takahashi and M. E. Gross, *J. Electrochem. Soc.*, **146**, 4499 (1999).
3. J. Zanghellini, S. Achenbach, A. El-Kholi, J. Mohr, and F. J. Pantenburg, *Microsystem Technol.*, **4**, 94 (1998).
4. S. K. Griffiths, R. H. Nilson, R. W. Bradshaw, A. Ting, W. D. Bonivert, J. T. Hachman, and J. M. Hruby, *Proc. SPIE*, **3511**, 364 (1998); SPIE-Int. Soc. Opt. Eng.
5. A. El-Kholi, J. Mohr, and R. Stransky, *Microelectron. Eng.*, **23**, 219 (1994).
6. K. J. Lee, J. Bucchignano, J. Gelorme, and R. Viswanathan, *J. Vac. Sci. Technol. B*, **15**, 2621 (1997).
7. T. Iwamoto, H. Shimada, S. Shimomura, M. Onodera, and T. Ohmi, *Jpn. J. Appl. Phys., Part 1*, **33**, No. 1B, 491 (1994).
8. H. Kuttruff, *Ultrasonics, Fundamentals and Applications*, Elsevier, New York (1991).
9. A. A. Busnaina, I. I. Kashkoush, and G. W. Gore, *J. Electrochem. Soc.*, **142**, 2812 (1995).
10. J. W. S. Rayleigh, *The Theory of Sound*, Dover, New York (1945).
11. W. L. Nyborg, in *Nonlinear Acoustics*, M. F. Hamilton and D. T. Blackstock, Editors, Chap. 7, Academic Press, London (1998).
12. J. Lighthill, Acoustic Streaming, *J. Sound Vib.*, **61**, 391 (1978).
13. K. Naugolnykh and L. Ostrovsky, *Nonlinear Wave Processes in Acoustics*, Cambridge University Press, Cambridge (1998).
14. P. J. Roache, *Computational Fluid Dynamics*, Hermosa Publishers, Albuquerque, NM (1976).
15. M. Tirrell, *Rubber Chem. Technol.*, **57**, 523 (1984).